Int. J. Heat Mass Transfer. Vol. 36, No. 2, pp. 277–286, 1993
Printed in Great Britain

0017–9310/93 $6.00 + 0.00

Electromagnetic vaporization of molten-metal drops

Y. BAYAZITOGLU and R. CERNY
Mechanical Engineering and Materials Science Department, Rice University, Houston, TX 77005, U.S.A.

(*Received* 3 *December* 1991 *and in final form* 7 *April* 1992)

Abstract—A one-dimensional heat conduction model is formulated to study electromagnetic vaporization of molten-metal drops as an initial attempt to model the physical process. Finite-element discretization is used to obtain the numerical solution, and numerical experiments are performed for three typical metals; aluminum, copper and titanium. Computational results show that the final size of the drop radius R_f can be effectively controlled by changing amplitude B_0 and radian frequency ω of the external alternating magnetic field. In addition, R_f remains almost constant for a relatively wide range of the initial drop radii R_0. The results of numerical solution are compared with the lumped solution and the differences in time history of the evaporation process studied.

1. INTRODUCTION

OVER THE last few years, there has been an increasing need for ultra-pure metals in the powder metallurgy industry where fine high-purity metal particles of a specified size are required. Classical methods of powder production are (see, e.g. refs. [1, 2]) usually unable to meet the three required conditions. References [3, 4] recommend the use of alternating magnetic fields to produce fine metal powders. An electromagnetic vaporization device is proposed there to produce metal powders of high-purity and given size.

Generally, mathematical modeling of interactions between an external alternating magnetic field and a liquid conductor involves the formulation of a magnetohydrodynamic problem involving mass, momentum and energy balances coupled with Maxwell equations (see, e.g. [5, 6]). In addition, the shape of the free-surface is to be determined.

Partial solutions of this general problem usually employ several different approaches. One of them emphasizes a precise determination of the magnetic field inside the body and the surrounding medium neglecting convection effects. It is then possible to express the power absorbed in the body and the Lorentz force in more or less general cases [7–9]. Another method concentrates on the problems of fluid dynamic aspects of levitation–melting processes and solves the velocity fields in liquid conducting bodies [10–12] and/or associated free-surface shape [13–15], under limiting assumptions for the external magnetic field. Another group of authors [14, 16] solve coupled hydrodynamic electromagnetic problems by neglecting changes of free-surface shape. Phase change processes are seldom solved in the general form and the assumption of a uniform temperature profile in the body is often made (see, e.g. ref. [14]). Melting processes are modeled more often than evaporation processes, in this area. Until now, evaporation of metals has not been the center of interest and the influence of electromagnetic fields has been sparsely investigated. A very simple lumped analysis of this problem has been made by Vutsens [17].

In the present paper, we emphasize energy-balance aspects of the vaporization process in an initial attempt to model the real physical process and deal with two limiting cases of the general problem. The model with conduction being the only mode of heat transfer within the droplet is one of them. The other limiting case is the lumped model assuming complete mixing within the droplet and therefore constant temperature inside. Any convective heat transfer effects within the droplet, in reality, will fall between these two limits.

2. ELECTROMAGNETIC VAPORIZATION DEVICE

Since ref. [3], which describes the electromagnetic vaporization device, is not readily available to the reader, we will briefly describe it here. Basic physical principles of electromagnetic heating of electrically conductive materials are well known and were mentioned in the previous section. With the electromagnetic vaporization device from ref. [3], these principles are applied to the size reduction of particles in metal powders.

The proposed prototype of this device (see Fig. 1) consists of an enclosure surrounded by a current carrying coil followed by a cooling chamber. Metal droplets coming from upper nozzles are heated to their vaporization temperature by the alternating magnetic field, then evaporated to a desired dimension and finally cooled until solid particles are obtained. The vaporization chamber can be filled with inert gas or evacuated.

The complete physical description of the system in the vaporization device is very complicated and

NOMENCLATURE

B	magnetic induction [T]
B_0	amplitude of magnetic induction [T]
B_t	threshold value of magnetic induction [T]
c	specific heat [J kg^{-1} K^{-1}]
$\mathbf{e}_z$	unit vector in the z-direction
g	acceleration due to the gravity [m s^{-2}]
h	heat transfer coefficient [W m^{-2} K^{-1}]
I	power density [W m^{-2}]
k	thermal conductivity [W m^{-1} K^{-1}]
k_e	thermal conductivity of the surrounding medium [W m^{-1} K^{-1}]
L_v	latent heat of vaporization [J kg^{-1}]
r	space coordinate [m]
$\mathbf{r}$	position vector [m]
R	radius of the drop [m]
R_f	final size of the drop radius [m]
R_0	initial size of the drop radius [m]
dR/dt	interface velocity [m s^{-1}]
s	relative space coordinate
t	time [s]
t_v	time of the evaporation duration [s]
T	temperature [K]
T_e	temperature of the surrounding medium [K]
T_m	melting temperature [K]
T_0	initial temperature of metal [K]
T_v	vaporization temperature [K]
ΔT_{max}	maximum overheating near the center of the sphere [K]
$v_{R,max}$	maximum interface velocity [m s^{-1}].

Greek symbols

β_e	volume thermal expansion coefficient of the surrounding medium [K^{-1}]
δ	skin depth [m]
ε	emissivity
μ	permeability of liquid metal [H m^{-1}]
μ_e	permeability of the surrounding medium [H m^{-1}]
ν_e	kinematic viscosity of the surrounding medium [m^2 s^{-1}]
ρ	density [kg m^{-3}]
σ	electrical conductivity [Ω^{-1} m^{-1}]
σ_{SB}	Stefan–Boltzmann constant [W m^{-2} K^{-4}]
ω	radian frequency [s^{-1}]
ω_t	threshold value of radian frequency [s^{-1}].

Subscripts

0	initial value
e	surrounding medium
m	melting
max	maximum value
SB	Stefan–Boltzmann
t	threshold value
v	vaporization
z	z-direction.

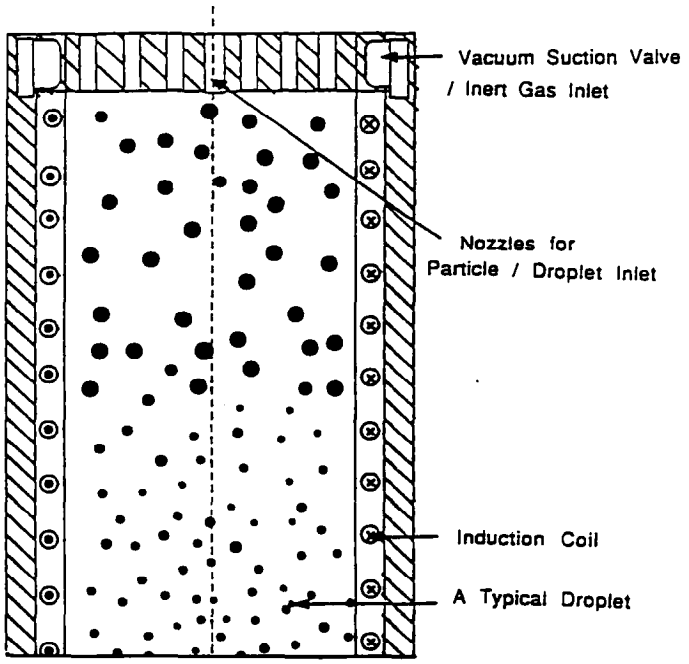

FIG. 1. Electromagnetic vaporization device.

demands a statistical approach to model the motion of particles in the electromagnetic field. Furthermore, each droplet by itself presents a coupled magneto-hydrodynamic problem. The medium surrounding the metal particles has to be modeled as a mixture of metal vapor and inert gas.

In this paper, we deal with very simplified mathematical formulations of the problem which enable us to identify some of the basic features of the vaporization device.

3. MATHEMATICAL MODEL OF ELECTROMAGNETIC VAPORIZATION

A spherical drop of molten-metal is placed in an external alternating magnetic field

$$\mathbf{B}(\mathbf{r}) = \mathbf{B}_0(\mathbf{r}) \cdot e^{j\omega t}. \tag{1}$$

Eddy currents induced in the drop heat the metal and if they are higher than a certain threshold value, the drop begins to evaporate and its radius decreases with time.

Assuming that the drop can change its size by evaporation only, the solution to this problem requires formulating a system of 11 equations representing volume balances of mass, momentum, and energy, coupled with Maxwell equations (see, e.g. ref. [6] for details) and three interface mass, momentum and energy balances (see, e.g. ref. [18]).

As one of the limiting solutions to the problem, we assume there is no convection heat and mass transport in the drop. This enables us to exclude mass and momentum balances and take into account the energy balance and Maxwell equations only. The consideration of an external uniform unidirectional alternating magnetic field of the form

$$\mathbf{B} = B_0 \cdot e^{j\omega t} \mathbf{e}_z \tag{2}$$

leads to a simple relation for power absorbed in the sphere as in ref. [19]. This leads us to represent heating due to the electromagnetic field as a source term in the energy balance equation and solve for energy transfer only.

Assuming that the local time variations of both the kinetic and potential energies are negligible when compared with the variation of internal energy, the influence of pressure on the energy balance is negligible and the internal energy density is a function of temperature only, we arrive at a heat conduction problem with a volume source term. Further, the phase change problem is based on the assumption that only surface evaporation occurs and neither heterogeneous nor homogeneous nucleation exists. We also assume that the drop radius is very small when compared with the characteristic dimensions of the vaporization device, and neglect interactions between droplets.

Finally, we assume that the surrounding medium is an inert gas at normal atmospheric pressure and the pressure of metal vapor remains constant for the duration of the process, in spite of metal evaporation. Thus, the influence of the surrounding medium can be expressed through boundary conditions only and we can use an equilibrium phase change model.

In our boundary conditions, assuming a stationary droplet (this is in accordance with the assumption that $B_0 = \text{const.}$) we take into account heat losses due to conduction, natural convection and radiation. The wall temperature is changing in the first phase of the process until the surface reaches the vaporization temperature. During vaporization, the wall temperature is assumed to be constant, according to our assumption of an equilibrium vaporization process.

Under these considerations, our model of electromagnetic vaporization of metals for the one-dimensional spherically symmetrical case is given by

$$\rho c \frac{\partial T}{\partial t} = \frac{1}{r^2} \frac{\partial}{\partial r}\left[r^2 \left(k \frac{\partial T}{\partial r} + I(r,t) \right) \right] \quad \text{in } \Omega = (0, R(t)\rangle \tag{3}$$

$$k\left(\frac{\partial T}{\partial r}\right)_{r=R(t)^-} = -\varepsilon\sigma_{SB}(T(R(t),t)^4 - T_c^4) - h(T(R(t),t) - T_c) \quad \text{at } T_m < T(R(t),t) < T_v \tag{4a}$$

$$\rho L_v \frac{dR(t)}{dt} = k\left(\frac{\partial T}{\partial r}\right)_{r=R(t)^-} + \varepsilon\sigma_{SB}(T_v^4 - T_c^4) + h(T_v - T_c) \quad \text{at } T(R(t),t) = T_v \tag{4b}$$

$$\lim_{r \to 0} \frac{\partial T}{\partial r} = 0 \tag{5}$$

$$R(0) = R_0 \tag{6}$$

$$T(r,0) = T_0, \quad T_m < T_0 < T_v. \tag{7}$$

The electromagnetic power density $I(r,t)$ in the drop has the form

$$I(r,t) = I(R(t),t) \cdot e^{(2/\delta)(r - R(t))} \tag{8}$$

where

$$\delta = \sqrt{\left(\frac{2}{\omega\mu\sigma}\right)}.$$

The power density $I(R(t),t)$ at the drop surface can be expressed according to ref. [19] in the form:

$$I(R(t),t) = \frac{3B_0^2 \cdot C(x)}{\sigma \cdot \delta D(x) \cdot E(x)} \tag{9}$$

where

$$C(x) = x^6(\sinh 2x + \sin 2x) - x^5(\cosh 2x - \cos 2x)$$

$$D(x) = x^2$$

$$E(x) = (\mu - \mu_e)^2 F(x) + 4(\mu - \mu_e)\mu_e \cdot G(x) + 4\mu_e^2 \cdot H(x)$$

$$F(x) = (2x^2 + 1)\cosh 2x + (2x^2 - 1)\cos 2x - 2x(\sinh 2x + \sin 2x)$$

$$G(x) = x^3(\sinh 2x - \sin 2x)$$

$$H(x) = x^4(\cosh 2x - \cos 2x)$$

$$x = \frac{R(t)}{\delta}.$$

The heat transfer coefficient h can be expressed in the free-convection limit by the relation from ref. [20]

$$h = \frac{k_c}{2R(t)}\left[2 + 0.392 \cdot \left(\frac{8\beta_c g(T(R(t),t) - T_c)\cdot R(t)^3}{\nu_c^2}\right)^{1/4}\right]. \quad (10)$$

4. NUMERICAL SOLUTION

Numerical methods to the solution of this type of problem are usually classified into three basic groups (see ref. [21]): front-tracking, front-fixing and fixed-domain methods. We choose a front-fixing method and introduce the Landau transformation [21]

$$s = \frac{r}{R(t)} \quad (11)$$

to convert the domain $\Omega = (0, R(t)\rangle$ into a fixed space interval $s = (0, 1\rangle$. Applying this transformation to our problem we obtain

$$\frac{\partial u}{\partial r} = \frac{1}{R}\frac{\partial u}{\partial s} \quad (12)$$

$$\left(\frac{\partial u}{\partial t}\right)_r = \left(\frac{\partial u}{\partial t}\right)_s - \frac{s}{R}\frac{dR}{dt}\frac{\partial u}{\partial s} \quad (13)$$

and equations (3)–(7) become

$$R\rho c\frac{\partial T}{\partial t} = \frac{1}{R}\frac{\partial}{\partial s}\left(k\frac{\partial T}{\partial s}\right) + \left(\frac{2k}{sR} + \rho c s\frac{dR}{dt}\right)\frac{\partial T}{\partial s} + \frac{2}{s}I + \frac{\partial I}{\partial s} \quad (14)$$

$$\frac{1}{R}k\left(\frac{\partial T}{\partial s}\right)_{s=1^-} = -\varepsilon\sigma_{SB}(T(1,t)^4 - T_c^4) - h(T(1,t) - T_c) \quad \text{at } T_m < T(1,t) < T_v \quad (15a)$$

$$\rho L_v\frac{dR}{dt} = \frac{1}{R}k\left(\frac{\partial T}{\partial s}\right)_{s=1^-} + \varepsilon\sigma_{SB}(T_v^4 - T_c^4) + h(T_v - T_c) \quad \text{at } T(1,t) = T_v \quad (15b)$$

$$\lim_{s\to 0}\frac{\partial T}{\partial s} = 0 \quad (16)$$

$$R(0) = R_0 \quad (17)$$

$$T(s,0) = T_0. \quad (18)$$

Computer implementation is done using the Galerkin finite-element method. Since the method is well known and widely used (see, e.g. ref. [22] for details) we do not explain every step of the procedure, and restrict our exposition to the main points, i.e. to the final results of the space and time discretization used. We use the standard finite-element notation $[\cdot]$ for matrices, $\{\cdot\}$ for column and $\langle\cdot\rangle$ for row vectors in what follows.

We denote by $\langle N\rangle$ the vector of the basis functions for the particular element A and put

$$\langle S\rangle = \frac{\partial\langle N\rangle}{\partial s}. \quad (19)$$

Denoting by $\{T\}^e$ the vector of nodal values of temperatures in one finite-element, we have

$$T = \langle N\rangle\{T\}^e. \quad (20)$$

The finite-element procedure gives the following system of nonlinear algebraic equations for one finite-element

$$[P]^e\frac{\partial\{T\}}{\partial t} + [H]^e\{T\} + \{F\}^e + \{B\}^e = \{0\} \quad (21)$$

where

$$[H]^e = [H_1]^e + [H_2]^e$$

$$[H_1]^e = \int_A \frac{k}{R}\langle S\rangle^T\langle S\rangle\,ds$$

$$[H_2]^e = -\int_A\left(\frac{2k}{sR} + \rho c s\frac{dR}{dt}\right)\langle N\rangle^T\langle S\rangle\,ds$$

$$[P]^e = \int_A \rho c R\langle N\rangle^T\langle N\rangle\,ds$$

$$\{F\}^e = -\int_A\langle N\rangle^T\left(\frac{2}{s}I + \frac{\partial I}{\partial s}\right)ds$$

$$\{B\}^e = -\left[\frac{k}{R}\langle N\rangle^T\langle S\rangle\{T\}\right]_{s_1}^{s_2}.$$

Using the element matrices and vectors to assemble the global ones for the whole domain $s = (0, 1\rangle$ we arrive at a system of equations in the form

$$[H]\{T\} + [P]\frac{\partial\{T\}}{\partial t} + \{F\} + \{B\} = \{0\}. \quad (22)$$

Performing the time discretization (see ref. [22]) by assuming that we know the nodal values $\{T\}_t$ at a time t and approximate $\{T\}_{t+\tau}$ in the time interval $\tau = \langle 0, \Delta t)$ using the linear relation

$$\{T\}_{t+\tau} = \frac{\Delta t - \tau}{\Delta t}\{T\}_t + \frac{\tau}{\Delta t}\{T\}_{t+\Delta t}. \quad (23)$$

Substituting equation (23) into equation (22) and applying the method of weighted residuals, we obtain the final recurrent form of the residual equations

$$[\bar{H}]\{T\}_{t+\Delta t} = [\bar{P}]\{T\}_t - \{F\}_t - \{B\}_t \quad (24)$$

where

$$[\bar{H}] = \tfrac{2}{3}[H] + \frac{1}{\Delta t}[P]$$

$$[\bar{P}] = -\tfrac{1}{3}[H] + \frac{1}{\Delta t}[P].$$

In the time-stepping procedure to solve equation (24) we use the local thermodynamic equilibrium condition

$$T(1, t) = T_v \tag{25}$$

as a boundary condition in equation (24) and the dynamic compatibility equation (15b) as a convergence criterion iterating for R and dR/dt.

One time step of our computational procedure can be described as follows:

(1) Put

$$R^1(t+\Delta t) = R(t)$$

$$\left(\frac{dR}{dt}\right)^1_{t+\Delta t} = \left(\frac{dR}{dt}\right)_t.$$

(2) Compute $\{T\}^1_{t+\Delta t}$ from equation (24) using

$$R^1(t+\Delta t), \left(\frac{dR}{dt}\right)^1_{t+\Delta t}.$$

(3) Compute $(dR/dt)^2_{t+\Delta t}$ from equation (15b) using $\{T\}^1_{t+\Delta t}$.

(4) If

$$\left| \frac{\left(\frac{dR}{dt}\right)^2_{t+\Delta t} - \left(\frac{dR}{dt}\right)^1_{t+\Delta t}}{\left(\frac{dR}{dt}\right)^1_{t+\Delta t}} \right| > \varepsilon$$

then set

$$\left(\frac{dR}{dt}\right)^1_{t+\Delta t} = \left(\frac{dR}{dt}\right)^2_{t+\Delta t}$$

$$R^1(t+\Delta t) = R(t) + \left(\frac{dR}{dt}\right)^1_{t+\Delta t} \cdot \Delta t$$

and go back to the point (2). Otherwise, put

$$\{T\}_{t+\Delta t} = \{T\}^1_{t+\Delta t}$$

$$\left(\frac{dR}{dT}\right)_{t+\Delta t} = \left(\frac{dR}{dt}\right)^1_{t+\Delta t}$$

$$R(t+\Delta t) = R^1(t+\Delta t)$$

and go to the next time step.

5. RESULTS OF NUMERICAL EXPERIMENTS

We simulated the vaporization process for copper, aluminum and titanium in argon surroundings. The thermodynamic and electrical parameters of liquid metals used in the model are shown in Table 1. Notice that because of the lack of experimental data for ε and k of Ti we adopted the value $\varepsilon = \varepsilon_s$ (700 K) from ref. [26] and determined $k(T)$ from the Wiedemann–Franz law (see, e.g. ref. [28]).

In the numerical experiments, we computed temperature fields $T(r, t)$ and time dependences of the drop surface position $R(t)$ and interface velocity $dR(t)/dt$ as functions of magnetic-field parameters B_0 and ω and the initial size of the drop radius R_0. The temperature of the surrounding medium T_s was 300 K in our computations, the initial sample temperature T_0 chosen just above the melting temperature T_m, i.e. metal was in the liquid phase at the beginning of the process.

Figures 2 and 3 present temperature profiles in the molten-titanium drop at characteristic times of the evaporation process for two initial drop radii that differ by one order of magnitude. Here, t_1 is the evaporation onset, t_2 a characteristic time in the initial phase of evaporation, t_3 the time when the maximum value of the overheating near the center of the sphere is reached and t_4 the time when vaporization ends.

Comparison of Figs. 2 and 3 shows marked differences in the heating process for varying R_0. In the case presented in Fig. 2, the initial drop radius R_0 is several times higher than the skin depth δ. Therefore, in the initial phase of heating, most of the Joule heat is absorbed in the thin layer under the drop surface and there is no overheating in the sphere until the temperature of the drop surface reaches the vaporization temperature T_v. Then, according to our model assumptions, the surface temperature is fixed at T_v and the temperature in the skin depth rises quickly, and marked overheating occurs in the sphere. The overheating causes thermal flux in the direction of the surface and according to relation (4b) increases the evaporation velocity. The interface velocity has then an increasing character for a relatively long time although the drop radius decreases rapidly as shown in Fig. 4 and the power absorbed in the sphere is reduced according to relation (9). This is due to the increase of overheating in the sphere and, naturally, the greater role of overheating in the vaporization process.

The rapid decrease of drop radius can lead to a situation when $\delta > R(t)$. The heating process is then qualitatively changing and getting an all-volume character. The overheating reaches its maximum value in the center of the sphere as shown in Fig. 2 but in the subsequent phase starts to decrease very rapidly due to a quick reduction of the absorbed energy in the drop. This fact follows from the interaction of the electromagnetic field with the conducting medium. When $\delta > R$ or even $\delta \gg R$, the sphere is in principle almost 'transparent' to the electromagnetic field. However, the occurrence of very high overheating inside the sphere during the volume-heating phase as documented in Figs. 2 and 3 leaves us in doubt whether such high values are realistic. Although we did not find any experimental data for homogeneous

Table 1. Thermodynamic and electrical parameters

Parameter	Cu	Al	Ti	Reference
$k(t)$ (W m^{-1} K^{-1})	166–183†	90.7–115†	$1.293 \times 10^{-2} T$	[23] for Cu, Al; [28] for Ti
c (J kg^{-1} K^{-1})	495	1080	700	[24]
ρ (kg m^{-3})	8000	2385	4110	[24]
$\sigma(T)$ (Ω^{-1} m^{-1})	5×10^6–2.95×10^6†	4.12×10^6–3.42×10^6†	5.81×10^5	[24]
T_m (K)	1356.5	933.2	1943	[25]
T_v (K)	1900	1800	2350	[29]
L_v (J kg^{-1})	4.73×10^6	1.078×10^7	8.79×10^6	[25]
ε	0.12	0.15	0.20	[26] for Cu, Ti; [27] for Al

† See table in ref.

nucleation temperatures and critical temperatures of metals in the literature, the occurrence of homogeneous nucleation at temperatures of 10 000 K and higher seems to be very probable. The peak character of the time history of the overheating leads us, in addition, to the assumption that there can be explosive evaporation inside the sphere.

Figure 3 contains characteristic temperature profiles in a Ti drop the initial radius of which is approximately two times lower than the skin depth. Here, volume heating occurs during the entire length of the evaporation process and, due to the character of heat conduction in the sphere, overheating begins even before the surface temperature reaches the vaporization temperature. The absolute values of overheating are lower than for the case of higher initial drop radius as shown in Fig. 3 and, therefore, the interface velocities are significantly lower. However, the final phase of the evaporation process is very similar to the one for higher initial drop radius. The overheating is very low, the interface velocity approaches zero and the drop radius converges to a certain limiting value. Figure 4 shows that at this limiting value, the final size of drop radius R_f almost does not depend on the initial value R_0 in a relatively large two order-of-magnitude range of R_0. For example, a comparison of results for $R_0 = 10^{-2}$ and 10^{-3} m shows differences smaller than 1.0% in R_f. This can be important from the point of view of technical applications, because the influence of homogeneous and especially heterogeneous nucleation (which is very probable in real metal samples) on the final size of the drop radius is then reduced.

The influence of external-magnetic field amplitude B_0 and radian frequency ω is seen from the form of equation (9). Numerical experiments showed order-of-magnitude differences in interface velocities, final sizes of drop radius and times of evaporation duration when B_0 and ω were changing. This is presented in Tables 2 and 3. The influence of ω was, according to theoretical assumptions, less than that of B_0.

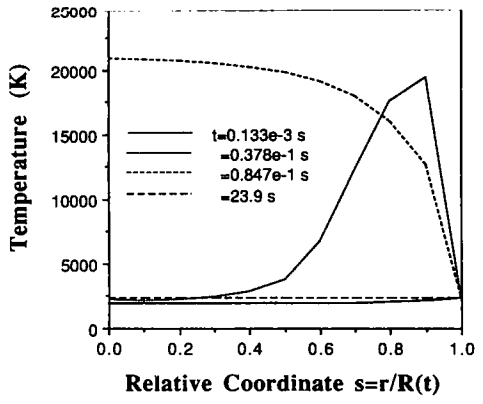

FIG. 2. Temperature profiles in the sphere for Ti, $B_0 = 5$ T, $\omega = 2\pi \times 10^5$ s^{-1}, $R_0 = 10^{-2}$ m, 0.133×10^{-3} s $\leqslant t \leqslant$ 23.9 s.

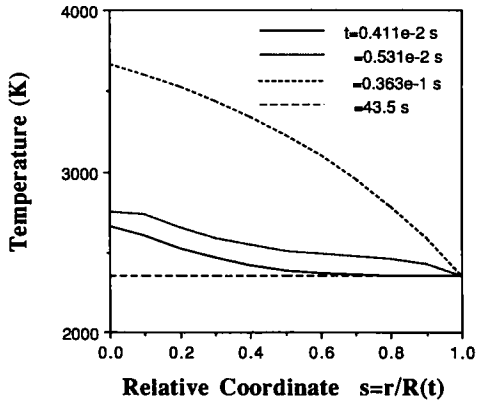

FIG. 3. Temperature profiles in the sphere for Ti, $B_0 = 5$ T, $\omega = 2\pi \times 10^5$ s^{-1}, $R_0 = 10^{-3}$ m, 0.411×10^{-2} s $\leqslant t \leqslant$ 43.5 s.

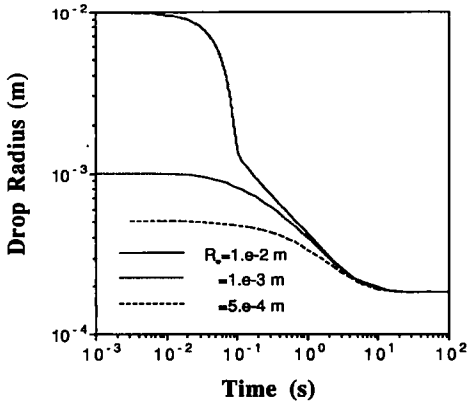

FIG. 4. Drop radius vs time for Ti, $B_0 = 5$ T, $\omega = 2\pi \times 10^5$ s^{-1}, 5.0×10^{-4} m $\leqslant R_0 \leqslant 10^{-2}$ m.

Table 2. Influence of the amplitude of external magnetic field B_0 for Al, $R_0 = 10^{-2}$ m, $\omega = 2\pi \times 10^5$ s^{-1}

B_0 [T]	R_f [m]	$v_{R,max}$ [m s^{-1}]	t_v [s]	ΔT_{max} [K]
0.05	1.48×10^{-3}	0.104×10^{-4}	2000	1.5
0.1	8.95×10^{-4}	0.543×10^{-4}	1220	5.8
0.5	3.35×10^{-4}	0.144×10^{-2}	247	142
1	2.24×10^{-4}	0.570×10^{-2}	118	546
10	6.28×10^{-5}	0.493	1.45	7848

Table 3. Influence of the radian frequency of external-magnetic field ω for Al, $R_0 = 10^{-2}$ m, $B_0 = 1.0$ T

ω [s^{-1}]	R_f [m]	$v_{R,max}$ [m s^{-1}]	t_v [s]	ΔT_{max} [K]
$2\pi \times 10^3$	3.79×10^{-3}	0.698×10^{-4}	2000	66
$2\pi \times 10^4$	8.84×10^{-4}	0.143×10^{-2}	1000	436
$2\pi \times 10^5$	2.24×10^{-4}	0.570×10^{-2}	118	546
$2\pi \times 10^6$	6.28×10^{-5}	0.190×10^{-1}	1.61	575
$2\pi \times 10^7$	1.85×10^{-5}	0.607×10^{-1}	0.321	575

The character of equations (4b) and (9) further leads us to conclude that threshold values of the magnitude and the frequency of external-magnetic field B_t, ω_t can be found for any combination of the two from the three remaining parameters B_0, ω, R_0. Comparison of B_t and ω_t for the three investigated metals Cu, Al, Ti, presented in Figs. 5 and 6, shows very small differences in the threshold values of Al and Cu but marked differences between these two metals and Ti. The higher values of B_t, ω_t for Ti are due to the higher vaporization temperature and higher skin depth of Ti.

The comparison of the characteristic parameters of the vaporization process for three mentioned metals, minimum value of the drop radius, maximum values of overheating and interface velocity and the time of evaporation duration shows the differences in R_f between Cu and Ti for the characteristic cases to be 50–55% while the difference between Cu and Al is approximately 2–3%. Similarly (as in the case of B_t and ω_t) the influences of the vaporization temperature, the skin depth, the emissivity and the heat transfer coefficient are also of key importance in reaching

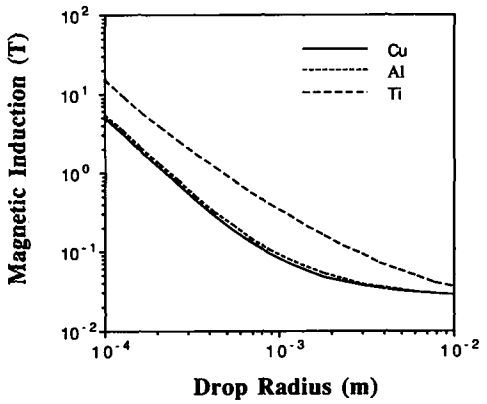

FIG. 5. Comparison of $B_t = f(R_0)$ for Cu, Al, Ti, $\omega = 2\pi \times 10^5$ s^{-1}.

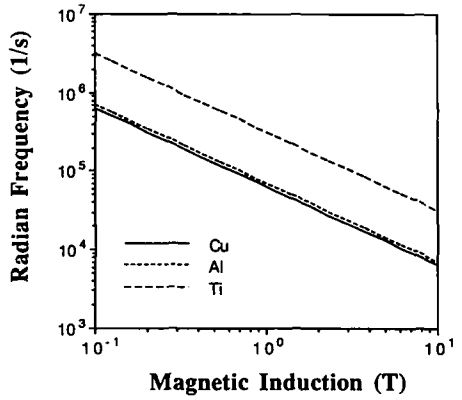

FIG. 6. Comparison of $\omega_t = f(B_0)$ for Cu, Al, Ti, $R_0 = 10^{-3}$ m.

the thermal equilibrium and stopping the vaporization process.

Figure 7 shows marked differences in ΔT_{max} between the three metals. The lowest values of ΔT_{max} were observed for copper, the material with the highest thermal diffusivity and lowest skin depth among the three metals; the highest ΔT_{max} for titanium with almost one-third of the value of the thermal diffusivity.

For lower values of the initial drop radius R_0, the highest values of interface velocities $v_{R,max}$ were observed for aluminum, the material with the lowest latent heat of vaporization per unit volume $\bar{L}_v = \rho L_v$. Here, the differences in ΔT_{max} between Ti and Al were relatively small and the contribution of the heat conduction term in equation (4b) to the interface velocity was therefore of the same order-of-magnitude for both metals. However, for higher R_0, Ti exhibited the maximum value of $v_{R,max}$. This fact is due to very high overheating in Ti for higher R_0, as shown in Fig. 7. For copper, the values of $v_{R,max}$ are always lower than the ones for aluminum due to significantly higher $\bar{L}_v$ of Cu. The maximum values of times of evaporation duration for the three compared metals were

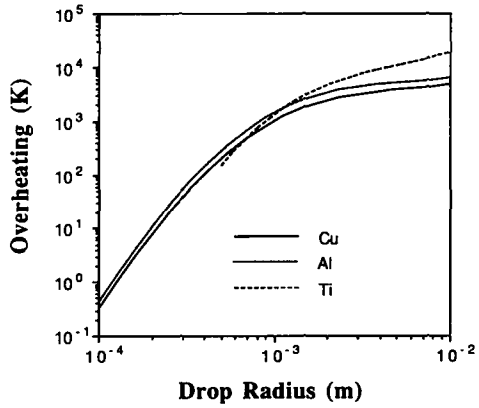

FIG. 7. Comparison of the maximum overheating near the center of the sphere for Cu, Al, Ti, $\omega = 2\pi \times 10^5$ s^{-1}, $B_0 = 5$ T, 10^{-4} m $\leqslant R_0 \leqslant 10^{-2}$ m.

observed for Ti and minimum values for Al. This can be explained by considering the low value of $\bar{L}_v$ of aluminum which increases the interface velocity in comparison with the other metals and highest skin depth of titanium which decreases dR/dt in the final phase of the vaporization process due to the reduction of the power absorbed in the material in this phase.

6. DISCUSSION

Figures 8 and 9 present a comparison of time histories of drop surface position and velocity computed with our conduction model and the lumped model including the relation from ref. [19] for the power absorbed in the sphere. The same Newton-type boundary conditions are used in both models.

As shown in Figs. 8 and 9, the marked differences between two compared models were observed for time histories of the vaporization process. Figure 8 shows the different character of the time dependence of interface velocities for both models. In the computations with the lumped model, the velocity has the highest value immediately after the beginning of the vaporization process and then decreases until vaporization ends.

The interface velocity obtained by the conduction model increases in the initial phase and then starts to decrease. Consequently, in the initial phase of vaporization, the velocities computed by the lumped model were higher, the differences were up to 90%. Later, the velocities computed by the conduction model reached the same value as for the lumped model and continued to increase. In this middle phase of the vaporization process, the conduction-model-computed velocities were up to 25% higher than for the lumped model. In the final phase of vaporization, lumped model velocities were a little higher, up to 10%.

The physical reason for these differences follows from the character of both models. The lumped model deals with the global volume energy balance. The time variation of interface velocity is therefore related to

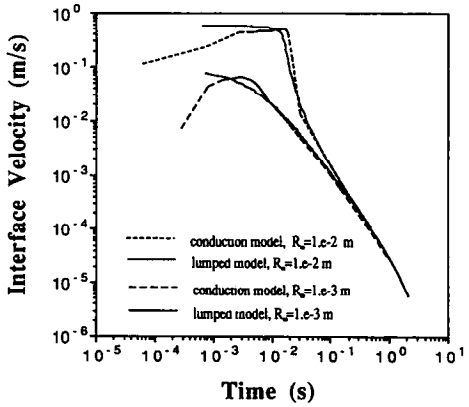

FIG. 8. Comparison of $dR(t)/dt$ computed by conduction model and lumped model for Al, $R_0 = 10^{-2}$ m, 10^{-3} m, $B_0 = 10$ T, $\omega = 2\pi \times 10^5\ s^{-1}$.

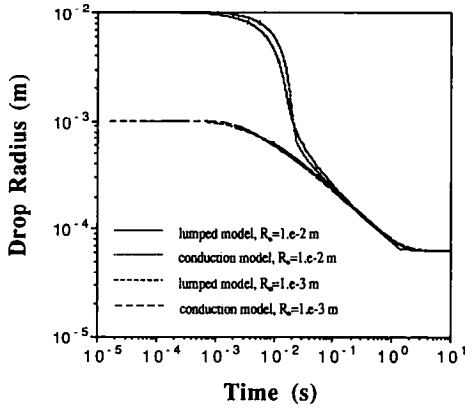

FIG. 9. Comparison of $R(t)$ computed by conduction model and lumped model for Al, $R_0 = 10^{-2}$ m, 10^{-3} m, $B_0 = 10$ T, $\omega = 2\pi \times 10^5\ s^{-1}$.

the global amount of energy absorbed in the sphere. The absorbed energy per unit surface area decreases with a decrease of the drop radius. Therefore, the interface velocity has to decrease also. In Fig. 8, the decrease of interface velocity with time was faster for the smaller drop. This is related to a faster attainment of the value of the drop radius comparable with the skin depth in this case.

In the equilibrium phase change model, the heating has a local character and the interface velocity depends on the negative temperature gradient at the surface. This temperature gradient starts to increase particularly after the vaporization temperature is reached at the surface, and, according to the assumption of an equilibrium vaporization process, the surface temperature is kept at a constant value. However, at the same time, a significant part of the heat absorbed in outer shells of the sphere flows in the direction to the center and increases the temperature inside the droplet. This is the reason why in the initial phase, the interface velocities are lower than with the lumped model. In the later phase, when the absorbed heat is significantly reduced due to the decrease of the drop radius under the skin depth, the vaporization process is driven by the heat accumulated inside. Apparently, this process is very fast due to the high thermal conductivity of the metal and the heat supply inside is spent in a relatively short time. In the final phase of evaporation, the overheating inside the sphere is very low and the state of thermal equilibrium with the surroundings is reached.

In Fig. 9, showing the comparison of curves (drop radius vs time) for both models, the differences between the models are not marked so well as the velocity differences from the previous figure due to the large region of R chosen. In the absolute values, the drop radius for the lumped model was in the initial phase up to 20% lower and in the subsequent phase up to 14% higher than with the conduction model. The differences were higher for higher initial drop radii. This is in accordance with the character of the

Table 4. Comparison of $R(t)$ computed by conduction and lumped models with experimental data of Vutsens [17]

t(s)	0	60	180	270	360
Experiment	8.25×10^{-3}	7.89×10^{-3}	7.21×10^{-3}	6.60×10^{-3}	6.08×10^{-3}
Conduction model $B_0 = 0.027$ T	8.25×10^{-3}	7.89×10^{-3}	7.15×10^{-3}	6.61×10^{-3}	6.06×10^{-3}
Lumped model $B_0 = 0.0275$ T	8.25×10^{-3}	7.87×10^{-3}	7.14×10^{-3}	6.59×10^{-3}	6.03×10^{-3}

heating process for both the models as described before.

However, in the final phase of vaporization, the state of thermal equilibrium was reached at principally the same value of the drop radius, the differences were only up to 1% which is comparable with numerical errors. This is apparently a logical conclusion following from the balance between heat gains and losses of the sphere.

We then compared results obtained by both conduction and lumped models with the experiments of Vutsens [17] performed for aluminum evaporated into vacuum with $\omega = 8\pi\times10^5$ s^{-1} and $T_v = 1700$ K. In this comparison, a fitting procedure to get the amplitude of the external-magnetic field B_0 was necessary because there was no information about B_0 in Vutsens' experiments. Table 4 shows a very good agreement of functions $R(t)$ computed by both conduction and lumped models with Vutsens' experiments for the initial phase of evaporation process (the differences are less than 1%).

Very small differences between the two models in this case are related to the fact that B_t is just above the vaporization threshold ($B_t = 0.016$ T, $B_0 = 0.027$ T) and that the intensity of electromagnetic heating is relatively small. Consequently, overheating inside the drop is very small and the differences between the two models almost vanish due to the large thermal conductivity of aluminum.

We further analyzed possible errors of our computations. Here, the influence of uncertainties in the values of liquid metal emissivity (which is not a well-documented parameter for higher temperatures) is apparently one of the most important. A 6% difference in the final size of the drop radius R_f was observed when simulations for $\varepsilon = 0.15$ and 0.30 were performed for aluminum, $B = 5$ T, $\omega = 2\pi\times10^5$ s^{-1}, $R_0 = 10^{-3}$ m. The influence of other material parameters is less important because they are determined with a higher precision. Neglect of forced convection might also cause significant errors in the computational results. The computations for a relative velocity between the droplet and ambient gas of 1 m s^{-1} showed a 10% difference in R_f when compared with the computations with $v = 0$ (again the case of Al, $B = 5$ T, $\omega = 2\pi\times10^5$ s^{-1}, $R_0 = 10^{-3}$ m was chosen).

Let us now go over some simplifying assumptions of our model. The influence of basic simplifications by neglecting convection and drop-shape change is apparent and was mentioned before.

Among the other assumptions, the constant vaporization temperature is equivalent to the application of an equilibrium phase change model and can be used for constant interface velocities, in general.

The assumptions of stationary drop and stagnant surrounding medium enabled us to consider a constant amplitude external-magnetic field and deal with heat losses due to conduction, natural convection and radiation. In general, a static approximation can be used for solenoids with a high ratio between the length and the radius where the magnetic field is near-homogeneous and for a relatively slow motion of droplets in the device. In accordance with the assumption of a stationary droplet we did not consider the inertia effects. In general, these effects are important for accelerating and decelerating media and are expressed in a momentum balance.

In modeling the heat conduction process, we used Fourier's law. It was not necessary to use the hyperbolic heat equation in our model. The estimated relaxation times for the three liquid metals Cu, Al, Ti [30, 31] are in the range of 10^{-11}–10^{-12} s, and our characteristic times are longer than 10^{-4} s. According to the general criterion for the dominance of wave behavior over diffusion [32], the influence of wave behavior on the heat propagation was at least six orders of magnitude less than diffusion.

The further assumption that heterogeneous nucleation can be neglected is valid only for a very pure material. In a real sample, impurities can occur in the metal and cause bubble formation inside the drop when temperatures are high enough. Homogeneous nucleation could arise at higher temperatures near the critical point. Also in this case it would be necessary to take into account the occurrence of bubbles in the overheated liquid.

Acknowledgement—This paper is based upon work supported by Texas Advanced Technology Program, under grant Nos 003604-008 and 003604-027.

REFERENCES

1. R. L. Sands and C. R. Shakespeare, *Powder Metallurgy*. George Newnes, London (1966).
2. W. Romanowski, *Highly Dispersed Metals*. Ellis Horwood, Chichester (1987).
3. Y. Bayazitoglu and F. R. Brotzen, Non-contact processing of materials at high temperatures, a proposal submitted to the Advanced Technology Program of Texas State Board of Higher Education, July (1991).
4. Y. Bayazitoglu and R. Cerny, Vaporization of molten-copper drops due to alternating electromagnetic field, an invited paper presented at the Int. Conf. Transport

Phenomena in Processing, Waikiki, Hawaii, 22–26 March 1992, to be included in the proceedings, to be published by Technomic.
5. P. G. Roberts, *An Introduction to Magnetohydrodynamics*. Longman, London (1967).
6. H. R. Cramer and S. I. Pai, *Magnetofluid Dynamics for Engineers and Applied Physicists*. McGraw-Hill, New York (1973).
7. E. Fromm and H. Jehn, Electromagnetic forces and power absorption in levitation melting, *Br. J. Appl. Phys.* **16**, 653–663 (1965).
8. P. R. Rony, The electromagnetic levitation of metals. In *Trans. Vac. Met. Conf. 1964* (Edited by M. A. Cocca), pp. 55–135. American Vacuum Society, Boston (1965).
9. G. Lohofer, Theory of an electromagnetically levitated metal sphere I: absorbed power, *SIAM J. Appl. Math.* **49**, 567–581 (1989).
10. H. K. Moffatt, On fluid flow induced by a rotating magnetic field, *J. Fluid Mech.* **22**, 521–528 (1965).
11. A. D. Sneyd, Generation of fluid motion in a circular cylinder by an unsteady applied magnetic field, *J. Fluid Mech.* **49**, 817–827 (1971).
12. A. D. Sneyd, Fluid flow induced by a rapidly alternating or rotating magnetic field, *J. Fluid Mech.* **92**, 35–51 (1979).
13. A. J. Mestel, Magnetic levitation of liquid metals, *J. Fluid Mech.* **117**, 27–43 (1982).
14. A. D. Sneyd and H. K. Moffatt, Fluid dynamical aspects of the levitation melting process, *J. Fluid Mech.* **117**, 45–70 (1982).
15. A. Gagnoud, J. Etay and M. Garnier, Free-surface determination in levitation melting process. In *Liquid Metal Flows: Magnetohydrodynamics and Applications* (Edited by H. Branover, M. Mond and Y. Unger), pp. 502–514. AIAA, Washington (1988).
16. A. Gliere, Y. Fautrelle and P. Masse, Numerical coupled model for electromagnetic stirring in continuous casting of steel. In *Liquid Metal Flows: Magnetohydrodynamics and Application* (Edited by H. Branover, M. Mond and Y. Unger), pp. 481–489. AIAA, Washington (1988).
17. A. P. Vutsens, Evaporation of a drop of molten metal suspended in a vacuum, *Magnetohydrodynamics* **6**, 579–581 (1970).
18. C. A. Miller and P. Neogi, *Interfacial Phenomena*. Marcel Dekker, New York (1985).
19. W. R. Smythe, *Static and Dynamic Electricity*, 3rd Edn. McGraw-Hill, New York (1968).
20. B. F. Armaly, T. S. Chen and N. Ramachandran, Correlations for mixed convection flows across horizontal cylinders and spheres, *J. Heat Transfer* **110**, 511–514 (1988).
21. J. Crank, *Free and Moving Boundary Problems*. Clarendon Press, Oxford (1984).
22. O. C. Zienkiewicz and R. L. Taylor, *The Finite Element Method*. McGraw-Hill, New York (1989).
23. Y. S. Touloukian, R. W. Powell, C. Y. Ho and P. G. Klemens, *Thermophysical Properties of Matter*, Vol. 1. IFI/Plenum, New York, Washington (1970).
24. E. A. Brandes (Ed.), *Smithells Metals Reference Book*, 6th Edn. Butterworths, London (1983).
25. D. E. Gray (Ed.), *American Institute of Physics Handbook*. McGraw-Hill, New York (1972).
26. Y. S. Touloukian and D. P. de Witt, *Thermophysical Properties of Matter*, Vol. 7. IFI/Plenum, New York, Washington (1970).
27. Properties and selection: nonferrous alloys and pure metals. In *Metals Handbook*, 9th Edn, Vol. 2. American Society for Metals, Metals Park, Ohio (1979).
28. E. U. Condon (Ed.), *Handbook of Physics*, 2nd Edn. McGraw-Hill, New York (1967).
29. S. Dushman, *Scientific Foundations of Vaccum Technique*, 2nd Edn. Wiley, New York (1962).
30. M. Chester, Second sound in solids, *Phys. Rev.* **131**, 2013–2015 (1963).
31. P. H. Francis, Thermo-mechanical effects in elastic wave propagation: a survey, *J. Sound Vibr.* **21**, 181–192 (1972).
32. D. Y. Tzou, On the thermal shock wave induced by a moving heat source, *ASME J. Heat Transfer* **111**, 232–238 (1989).